

Thermal Aging Phenomena in Cast Duplex Stainless Steels

T.S. BYUN,^{1,3} Y. YANG,² N.R. OVERMAN,¹ and J.T. BUSBY²

1.—Nuclear Sciences Division, Pacific Northwest National Laboratory, Richland, WA 99352, USA.
2.—Materials Science and Technology Division, Oak Ridge National Laboratory, Oak Ridge, TN 37831, USA. 3.—e-mail: thaksang.byun@pnnl.gov

Cast stainless steels (CASSs) have been extensively used for the large components of light water reactor (LWR) power plants such as primary coolant piping and pump casing. The thermal embrittlement of CASS components is one of the most serious concerns related to the extended-term operation of nuclear power plants. Many past researches have concluded that the formation of Cr-rich α' -phase by Spinodal decomposition of δ -ferrite phase is the primary mechanism for the thermal embrittlement. Cracking mechanism in the thermally-embrittled duplex stainless steels consists of the formation of cleavage at ferrite and its propagation via separation of ferrite–austenite interphase. This article intends to provide an introductory overview on the thermal aging phenomena in LWR-relevant conditions. Firstly, the thermal aging effect on toughness is discussed in terms of the cause of embrittlement and influential parameters. An approximate analysis of thermal reaction using Arrhenius equation was carried out to scope the aging temperatures for the accelerated aging experiments to simulate the 60 and 80 years of services. Further, an equilibrium precipitation calculation was performed for model CASS alloys using the CALPHAD program, and the results are used to describe the precipitation behaviors in duplex stainless steels. These results are also to be used to guide an on-going research aiming to provide knowledge-based conclusive prediction for the integrity of the CASS components of LWR power plants during the service life extended up to and beyond 60 years.

INTRODUCTION

Cast stainless steels (CASSs) are highly corrosion-resistant Fe-Cr-Ni alloys with mostly austenite(γ)–ferrite(δ) duplex structure and have been used for a variety of large components in nuclear power plants, such as valve bodies, pump casings, primary coolant piping, and elbows.^{1–9} The CASSs are one of the most important alloy groups in light water reactor (LWR) systems as only the casting technologies, i.e., static and centrifugal castings, enable the fabrication of such large components with proper resistance to environmental attacks. Many primary components experience both reactor coolant and radiation environments exposing to elevated temperatures, internal pressures, and corrosive environments.¹ Since a massive amount of CASS components are installed in each modern nuclear power plant, any significant degradation in mechanical properties, static and dynamic fracture toughnesses, for instance, of CASS components will

raise a serious concern on the integrity of entire power plant. Upon the presumption that the replacement cost of such massive components is prohibitive, thorough scientific understanding and systematic monitoring the thermal aging degradation of CASS components should therefore be essential requirements for assessing the plant safety.

Relatively few critical degradation modes of concerns are expected within the current design lifetime of 40 years, given that the CASS components have been processed properly.^{1–5} Further, there is little concern for CASS components related to general or localized corrosion, fatigue, flow-accelerated corrosion, or wear for current lifetimes.^{1,8} On the integrity of CASS components beyond the current timeframe of 40 years, however, no conclusive prediction can be made as currently no direct experience with these materials exists. Further, numerous aging experiments in the past have been performed at or above 400°C to investigate microstructural evolution and mechanical behaviors

and to predict long-term CASS behaviors.^{2-7,10-22} However, such highly-accelerated aging treatment above the operation temperature range is yet to be thoroughly validated for simulation of the lower temperature ($\sim 300^\circ\text{C}$) phenomena in the current fleet of nuclear power plants.⁹

The current consensus might be that, although the vast majority of the current nuclear power plants are expected to be operational for extended lifetimes of 60 years or potentially longer,¹ the behaviors of CASS alloys during such prolonged periods have remained largely unknown. Therefore, an assessment of property degradation during such long-term thermal aging is believed to be essential for extended-term services because a rupture of the primary pressure boundary could lead to a severe loss-of-coolant accident and possible exposure of the public to radiation.²³ This article is intended to provide an overview summary on the current understanding of thermal aging phenomena. Discussion will be made by combining the results of past and on-going studies.

CAST DUPLEX STAINLESS STEELS AND THERMAL EMBRITTLEMENT

Cast Austenitic–Ferritic Stainless Steels

A variety of cast stainless steels have been used in nuclear power plants as reactor models, and material selections have evolved with the time of construction. The CASS alloys are typically graded by their chemistries and microstructural constituents,²⁴⁻²⁶ and the most common CASSs used in nuclear power plants are the duplex austenitic(γ)–ferritic(δ) alloys, which include the CF family of cast grades with normally $\sim 19\%$ Cr and $\sim 10\%$ Ni. In the CASS grades, the main alloy elements, i.e., Fe, Cr, Ni, Mn, Si and C, and cooling rate ultimately determine their microstructure, in particular, the volume fractions of ferrite (δ) and austenite (γ) phases. The nuclear grade CASS alloys, CF3 and CF3M, for example, contain 3–30% ferrite in the austenite matrix; some CF8 alloys contain only about 10% ferrite in volume while the CF3 alloys typically have higher amount of ferrite, 10–20%. The amount of ferrite is a critical factor in the mechanical properties as well as in the aging process, as higher aging degradation is usually associated with high ferrite content, in particular with $>20\%$ ferrite where a near-complete network of ferrite can be achieved.^{3,27,28}

More ferrite content generally leads to a higher tensile strength due to its intrinsic strength and more precipitates, while the austenite phase usually has higher ductility and less precipitates. The most common alloys in nuclear power plants include the A351-CF3 and A351-CF8 series of alloys with CF3, CF3A, CF3M, CF8, CF8A, and CF8M being the most prominent variants.¹⁻⁹ Typical nuclear power plants have been using CF8A, CF8M, and CPF3M for their reactor coolant and auxiliary system piping

(note: A-anneal, M-molybdenum-doped, and P-piping). Many reactor coolant pump casings are made of grade CF8, CF8A, or CF8M CASSs. Reactor coolant valve bodies and fittings often use CF8A or CF8M. In later construction applications and replacements, the CF3s with lower carbon content ($<0.03\%$) have been used rather than CF8s ($C < 0.08\%$). This is because lower carbon content is favored for forming less δ -ferrite and fewer carbide particles at boundaries and interfaces. Table I lists the chemistries of four common CASS alloys, which are also used as model alloys in the on-going research.⁸ Primarily controlled chemical elements in the CASSs are carbon and molybdenum; CF3 and CF3M have lower carbon contents <0.08 wt.% and CF3M and CF8M are alloyed with 2–3 wt.% Mo.

A typical duplex ferrite–austenite microstructure taken with SEM and five SEM–EDS maps for key alloy elements are displayed in Fig. 1. These images are from a CF3 model alloy block containing 15 vol.% δ -ferrite and 85 vol.% austenite phases. This γ – δ duplex structure is formed during cooling: the melt phase solidifies to a δ -ferritic grain structure and then the majority of the body-centered cubic (bcc) ferrite transforms to the face-centered cubic (fcc) austenite during cooling. Since only minor part of the δ -ferrite is retained around the austenite grain boundaries after cooling, many of the ferrite islands are small and round or long and narrow at low volume fractions of $<\sim 10\%$ and the ferrite area become a well-connected network as its volume fraction increases above $\sim 20\%$. It is also a common observation that the shape of ferrite phase and its volume fraction vary significantly with sampling location in an ingot.

The EDS maps in Fig. 1, in which brighter colors indicate higher elemental contents, show elemental partitioning between austenite and ferrite phases; the ferrite stabilizers (Fe, Cr, and Mo) are enriched in ferrite while Ni favors the austenite phase. Although silicon seems to be only slightly enriched in ferrite, higher silicon content should result in higher ferrite amount in the duplex structure. As will be discussed later, along with the crystallographic difference, i.e., bcc versus fcc, the elemental partitioning leads to a significant difference in precipitation behaviors between the two constituent phases during thermal aging.

Mechanical Property Degradation

Typically, the thermal aging of a cast stainless steel can cause a mild change in strength, decrease in ductility and fracture toughness, and a positive ductile–brittle transition temperature shift (ΔDBTT). Since much of the hardening due to the formation of various fine precipitates can be compensated by the softening effect from thermal relaxation and δ -phase decomposition, strength change is relatively less profound than those of

Table I. Chemistries of model cast stainless steels (and their wrought equivalents) and ASTM specification²⁶ in wt.% or ppm (for P, C, S, and N) and their ferrite mole fraction data

Grade	Fe	Cr	Ni	Mn	Mo	Si	Cu	Co	P	C	S	N	Mol.%
CF3 (304L)	Bal.	19.2	8.1	1.44	0.34	0.99	0.41	0.18	290	262	324	1020	7.7
(Specification)		17–21	8–12	<1.5		<1.5			<400	<300	<400		
CF3M (316L)	Bal.	19.3	9.8	1.14	2.30	1.22	0.28	0.15	330	284	253	838	11.8
(Specification)		17–22	9–13	<1.5	2–3	<1.5			<400	<300	<400	1000–2000	
CF8 (304)	Bal.	18.7	8.9	1.10	0.29	1.27	0.29	0.15	260	665	376	606	6.9
(Specification)		18–21	8–11	<1.5		<2			<400	<800	<400		
CF8M (316)	Bal.	18.5	10.4	0.65	2.33	1.02	0.33	0.17	310	433	243	1020	12.3
(Specification)		18–21	9–12	<1.5	2–3	<2			<400	<800	<400		

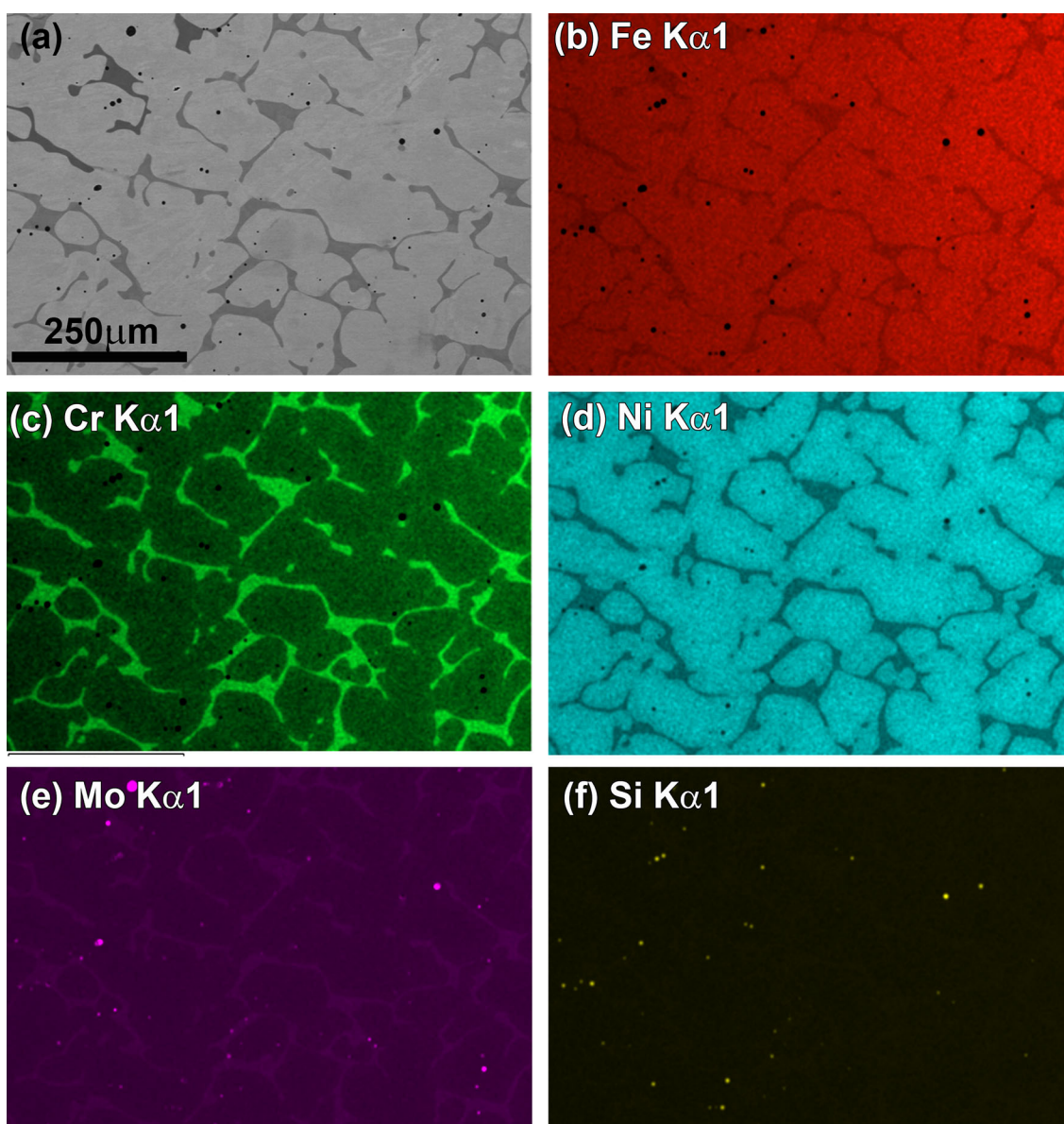


Fig. 1. A SEM image (a) and SEM-EDS maps (b–f) of CF3 alloy showing austenite-ferrite duplex microstructure and elemental partitioning. Note that this imaged area contains 15% ferrite and 85% austenite phases, and that brighter colors indicate higher elemental contents in the EDS maps.

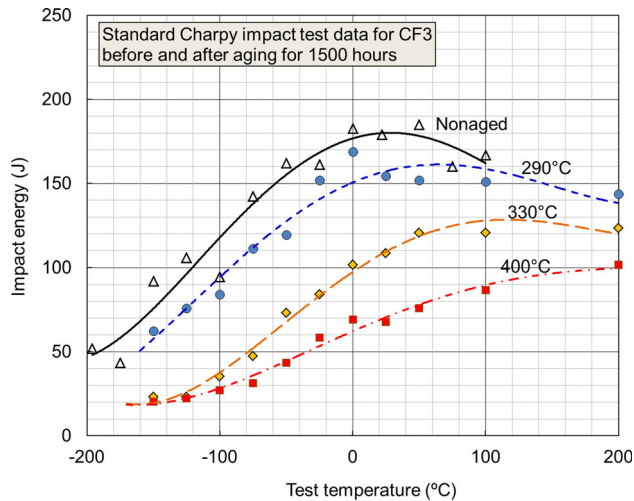


Fig. 2. Aging temperature dependence of Charpy impact energy in CF3 alloy after aging for 1500 h.

ductility and toughness.³ The biggest concern for an extended-term service has been their susceptibility to the thermal aging-induced embrittlement at reactor operating temperatures ranging from 280°C to 340°C. Therefore, the vast majority of past researches have focused on the reduction of crack or notch toughness in CASS components.¹⁻⁹

Earlier investigations performed in Argonne National Laboratory have suggested that the thermal embrittlement can occur in cast stainless steel components during the common reactor design lifetime of 40 years.^{2-7,9} However, a complete embrittlement (or zero ductility) above room temperature has not been observed in the thermally aged CASS alloys for LWR conditions. Many past studies have been carried out at temperatures higher than the common operating temperature range, i.e., in accelerated aging conditions, to obtain detectable property change within short time periods,^{2-7,10-22} and it has become customary to simulate the microstructural processes in aging during service by aging at 400°C.¹⁰⁻²² However, as a variety of aging mechanisms are found to strongly depend on aging temperature, we need to be conscious on the relevance of those accelerated aging experiments to the actual service conditions in LWR power plants. The standard impact test data displayed in Fig. 2 confirm that the effect of aging on impact energy is highly sensitive to aging temperature. This dataset after a relatively short aging for 1500 h also demonstrates that the toughness degradation, measured by the shift of DBTT and decrease of upper shelf energy (USE), occurs in early aging: the 400°C aging case has experienced a significant DBTT increase of ~100°C and a USE reduction of ~80 J.

Mechanism of Thermal Embrittlement and Influential Factors

As in any commercial steels, it is expected that the degree of aging embrittlement in CASS alloys depends on the grades and heats of the materials. As summarized in the latest reports,^{2-7,9} the low-carbon CF3 steels were generally more resistant to the thermal embrittlement than other alloys, while the Mo-bearing, high-carbon CF8M steels are among the least embrittlement-resistant alloys. Primary brittle fracture mechanisms observed in the thermally embrittled duplex stainless steels were the cleavage of ferrite and the separation of the ferrite/austenite phase boundary.²⁻⁷ Indeed, the embrittlement is caused by thermally-induced changes in microstructure. For cast stainless steels, the main microstructural mechanisms of thermal aging at <500°C are associated with the precipitation of additional phases in the ferrite: (a) formation of a Cr-rich α' -phase through Spinodal decomposition, (b) precipitation of a G-phase (Ni, Si-rich) and $M_{23}C_6$ carbide, and (c) additional precipitation and/or growth of existing carbides and nitrides at the ferrite/austenite phase boundaries.^{2-9,13,17,19,29-36}

In the austenite matrix phase, thermal aging induces various precipitations but usually causes a negligible to moderate effect on the mechanical properties of the phase.³⁻⁷ The effect on toughness, in particular, is less pronounced in the austenitic phase. This is not only because precipitation kinetics is relatively slow in austenite but also because the austenite itself retains enough ductility with precipitates and the property change. In contrast, the formation of Cr-rich α' phase and Fe-rich α -phase by Spinodal decomposition of the ferrite (δ) phase is known to be the primary mechanism for thermal embrittlement.^{2-7,9,29} The α' -phase particles can harden the ferrite matrix but reduce the capability of plastic deformation before final fracture as well as the cracking resistance in ferrite. In a ferritic/austenite duplex structure, the ferrite with extra hardening may fail in brittle mode but the surrounding austenite can provide some ductility. A highly embrittled case can be observed with a high contiguity of ferrite phase or with high ferrite content.²⁻⁷ Further, the ferrite/austenite phase boundary provides an easy path for crack propagation in high-C or high-N steels because of the excessive carbides or nitrides formed at boundaries.²⁻⁴ The decrease in room temperature (RT) Charpy impact energy by thermal aging at 400°C indicated that the RT impact energy reaches a minimum saturated value.⁴⁻⁷ The actual value of the saturated RT impact energy for a specific cast stainless steel is independent of aging temperature but depends strongly on the chemical composition of the steel: it is lower for the Mo-bearing CF8M steels than for the Mo-free CF3 or CF8 steels, and decreases with ferrite content and the concentration of C or N.

The aging time at 400°C measured at the same reduction of impact energy in different heats varied by more than two orders of magnitude.²⁻⁷ In general, an aging mechanism with high activation energy can cause fast embrittlement, and the materials with the same chemical composition but different processing routes show different kinetics of embrittlement.⁶ The cast stainless steels with low activation energy and slow embrittlement at 400°C show G-phase precipitation after aging, and steels with high activation energy and fast embrittlement at 400°C do not contain G-phase.^{2-7,29} The primary embrittlement mechanism, the Spinodal decomposition of ferrite, should have higher activation energy because of the short range and fast characteristics of the process.^{3,7,17,19,31,32,35} The strengthening in ferrite is caused primarily by Spinodal decomposition of ferrite to form the Cr-rich α' -phase, and consequently the kinetics of thermal embrittlement should be primarily controlled by the size and spacing of the α' -phase.

Except for the material conditions, the aging temperature should be the most determining parameter for the kinetics of thermal embrittlement, as indicated in Fig. 2. As discussed above, the aging embrittlement depends on many materials and environmental parameters, including chemistry, processing condition, aging temperature, and irradiation condition.^{1-7,37-40} Practically, the wide range of impact energy data influenced by the parameters mentioned above may not allow an integration into single figure in a discernible way. Instead, a schematic illustration was constructed to express a summary of the reviewed context above: Fig. 3 illustrates the general degradation in toughness using the Charpy impact energy at room temperature. Among the parameters, the ferrite fraction and alloy elements (Cr, Si, C, and N) are materials internal parameters while aging temperature and irradiation are external ones, all of which commonly reduce the absorbed energy. Other major elements in CASSs, such as Ni, Mo, and Mn, also accelerate or decelerate the embrittlement process depending on the alloy,⁴ which are not displayed in the figure. It is also well known that thermal aging has a synergistic effect with irradiation when the CASS components are used in or near a reactor.³⁷⁻⁴⁰ The effect is included in Fig. 3 although no detailed discussion is provided in this article. Finally, the lowest impact energy from the embrittled steels is set at 20 J but may vary with alloys.

SCOPING CALCULATION FOR ACCELERATED AGING

Since it is practically not possible to pursue a real-time aging experiment for the extended life time of 60 years or more, accelerated aging experiments have been carried out for much shorter periods, e.g., 3 years. A key principle in choosing the aging temperature and time should be that the aging

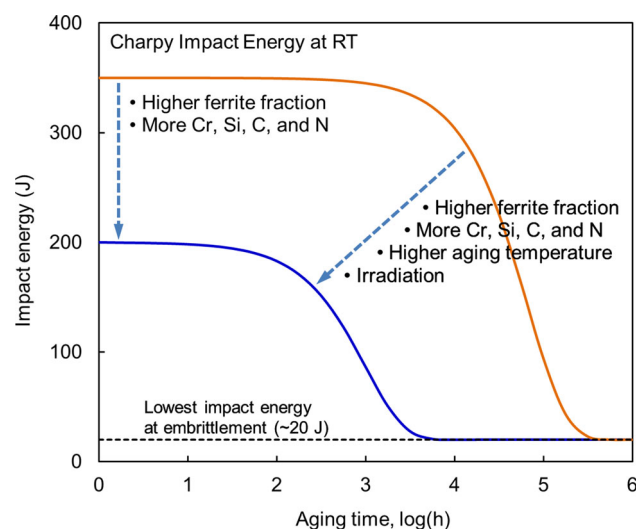


Fig. 3. Schematic of embrittlement process, i.e., the dependence of impact energy versus aging time curve on various variables.

mechanisms at the elevated temperatures must not differ from those found in the CASS service temperature range of 280–340°C. A low risk approach might be to choose an accelerated aging temperature as close to the service temperature as possible; however, the aging time should be reasonably short. In this section, a calculation based on a simple thermal activation model is performed to approximately scope the temperature and time for the accelerated aging treatments.

In scoping analysis, the thermal activation energy is the key parameter for using the common activation model of an Arrhenius-type equation. The activation energies obtained for the CF3, CF8, and CF8M alloys from impact energy changes were in a wide range of 75–250 kJ/mol, which agreed with the values from the plot of G-phase volume fraction.⁷ However, even if the same microstructural mechanisms occur in both the service and the accelerated aging experiment, the relative contributions of those mechanisms will change with temperature and thus the mechanism-averaged activation energy should vary with aging temperature. Therefore, a measurement of apparent activation energy based on the physical property should be considered as the average of multiple activation energies corresponding to multiple mechanisms. Indeed, the activation energy for thermal embrittlement is not constant over the interested aging temperature range of 290–450°C.²⁻⁷ It should be known that a complete embrittlement of CASSs cannot occur or the degradation progresses very slowly in the reactor operating temperature range. With multiple microstructural processes in play, therefore, an extrapolation of data obtained for high temperatures $\geq 400^\circ\text{C}$ to predict the extent of thermal embrittlement at reactor temperatures ($\sim 300^\circ\text{C}$) cannot be easily justified. The following thermal activation analysis will be based on the assumption

that the activation energy for thermal embrittlement can be represented by an average value in the temperature range of 290–400°C.^{3,7}

In addition, the activation energy (Q) measured by a specific mechanical property change, such as the increase of hardness or decrease of toughness, may not accurately represent the microstructural progresses in CASSs, because those macroscopic properties can include both negative and positive effects from the detailed aging processes. Some precipitation mechanisms may soften the phase, which generally helps increase fracture toughness, but provide new crack initiation sites and help lowering toughness value. For instance, some Charpy-impact datasets yielded activation energies in the range of 75–100 kJ/mol, which is well below the value of ~ 240 kJ/mol for chromium bulk diffusion, which has been assumed to be rate-controlling in the low-temperature decomposition of the ferritic phase.^{7,41} The activation energies for the diffusion of metallic elements in the ferrite phase are in the range of 210–250 kJ/mol.^{41,42} This Q -range should approximately represent the Spinodal decomposition process to form α' and α phases in various conditions. It has also been shown that the activation energies measured for the Spinodal decomposition and G-phase precipitation were very similar, and a value of 243 ± 80 kJ/mol was obtained for both mechanisms.³⁹

Recognizing that the aforementioned complexities can lead to significant uncertainties in determining accelerated aging temperatures, a calculation has been performed for a wide range of activation energy, 100–300 kJ/mol, to take into account possible variations in aging mechanisms within the aging temperature range.^{3,6,7,39} To calculate the aging time $t(T)$ in an accelerated aging experiment at an elevated temperature T , the Arrhenius-type equation is used:⁷

$$t(T) = t_0 \left[e^{Q/RT} / e^{Q/RT_0} \right] \quad (1)$$

where t_0 and T_0 are the time and temperature for service lifetime, respectively, and Q is the activation energy (in kJ/mol) and R the gas constant (8.314 J/mol K). The t_0 was set at 60 years or 80 years and T_0 at 300°C.

Figure 4a and b displays the aging time versus aging temperature curves in semi-log coordinates for the accelerated aging experiments to simulate, respectively, 60 years and 80 years of services. First of all, these data state that the temperature dependence of aging time varies widely with activation energy. For a mechanism with the activation energy of 250 kJ/mol, for example, a CASS needs to be aged at about 328°C, a 28°C increase from the representative service temperature (300°C), to complete the simulated aging for a service of 60 years in 5 years. For the same degree of effect, aging at about 377°C for 5 years is needed for the mechanism with an

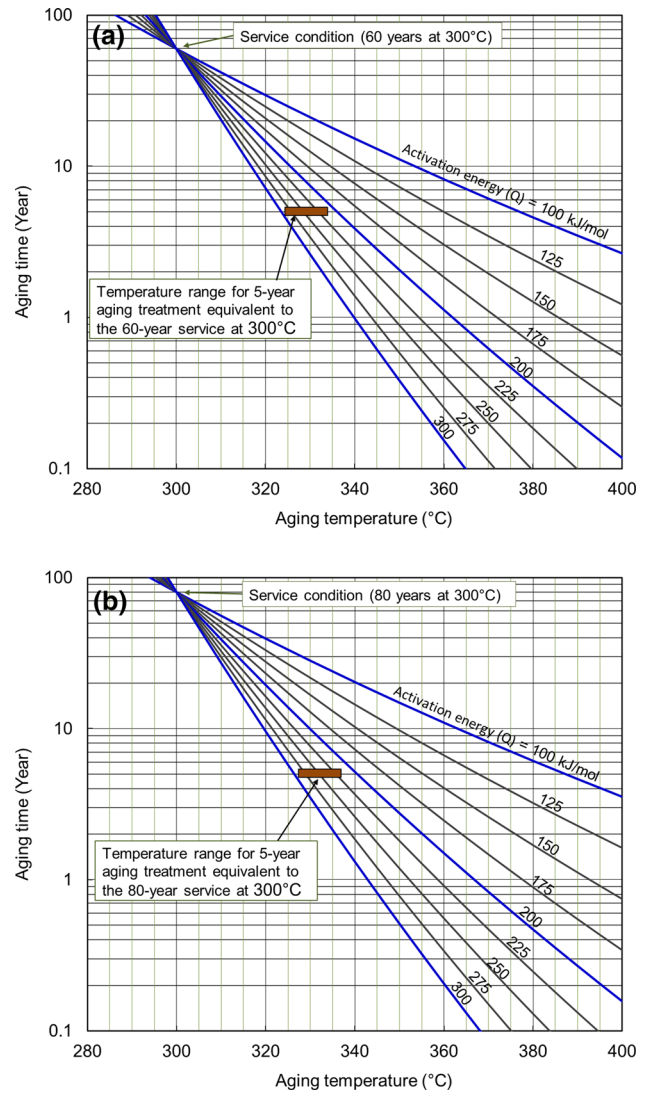


Fig. 4. Semi-log plots of aging time versus aging temperature data for different activation energies. The rectangular bars indicate aging temperature ranges for accelerated (higher temperature) aging treatments to simulate (a) 60- and (b) 80-year operations at 300°C, respectively.

activation energy of 100 kJ/mol. A rectangular band marked at 5 years is to range the aging temperature for the aging mechanisms caused by the diffusion of metallic elements: $\sim 330 \pm 5^\circ\text{C}$ is the aging temperature range for 210–280 kJ/mol. It is easily seen in Fig. 4b, which simulates an 80-year service at 300°C, that these aging temperatures are shifted by less than $+5^\circ\text{C}$ from those in Fig. 4a; the aging at $\sim 335 \pm 5^\circ\text{C}$ for 5 years simulates the 80-year service as indicated at the middle of the rectangular band. For an accelerated aging experiment, therefore, the lowest aging temperature should be $\sim 330^\circ\text{C}$ to achieve the reasonable degradation level representing 60 years and 80 years in a 5-year time frame.

THERMODYNAMIC CALCULATION OF PRECIPITATION BEHAVIOR

Precipitation processes in cast stainless steels will be slow at temperatures $\leq 400^\circ\text{C}$ and are predicted to not reach a complete equilibrium in the design life of LWRs. Preliminary kinetics calculation and mechanical test data, however, indicated that an equilibrium calculation can approximately predict the microstructural status that a long-term thermal aging can produce, except for the intermediate phases existing for a limited period. In this research, an extended equilibrium calculation was carried out for the model alloys (CF3, CF3M, CF8 and CF8M) using the CALPHAD method with database and software options of OCTANT and PANDAT.^{43–45} This calculation was intended to obtain the equilibrium precipitation data that can also provide baseline information for guiding further investigations on aging phenomena. In the calculation, only the major alloy elements, Fe, Cr, Ni, Mo, and Si, and key trace elements, C and N, were taken into account. For each alloy, a two-step calculation was conducted to obtain phase equilibrium data under the assumption of thermodynamic equilibrium conditions. The first step was to generate data on phase fraction versus temperature from 1600°C to 1200°C , which approximately simulates the melting and cooling in the casting process. Since the optical microscopy data were provided for the amount of ferrite phase, the result of the first step calculation was used to determine the chemical compositions of the austenite and ferrite phases at the moment when the specified (i.e., measured) amount of ferrite was formed during casting. The second step was to calculate the precipitate phase fraction versus temperature in the temperature range of $250\text{--}450^\circ\text{C}$ for both the austenite and ferrite phases using the composition data from the first step. The calculation was performed under the assumption that no austenite–ferrite transformation occurs in the aging temperature range, although significant phase changes occur in the form of precipitation within respective phases.

Figures 5 and 6 display the calculation results for equilibrium precipitates in austenite and δ -ferrite, where the mole fractions of precipitate phases in CASSs are given as functions of the aging temperature. Multiple known phases were predicted to precipitate in the duplex-phase structure in equilibrium condition. It is noted that the major precipitates, σ and α' phases, are dominantly formed in austenite and ferrite, respectively, while other minor phases are formed commonly in both matrix phases. That is, the equilibrium precipitates formed in austenite (Fig. 5) are σ -phase, G-phase, chromium nitride (Cr_2N), Laves (η) phase, M_{23}C_6 carbide, and π -phase, while those in ferrite (Fig. 6) are α' -phase (Spinodal decomposition product), G-phase, Laves (η) phase, chromium nitride (Cr_2N), M_{23}C_6

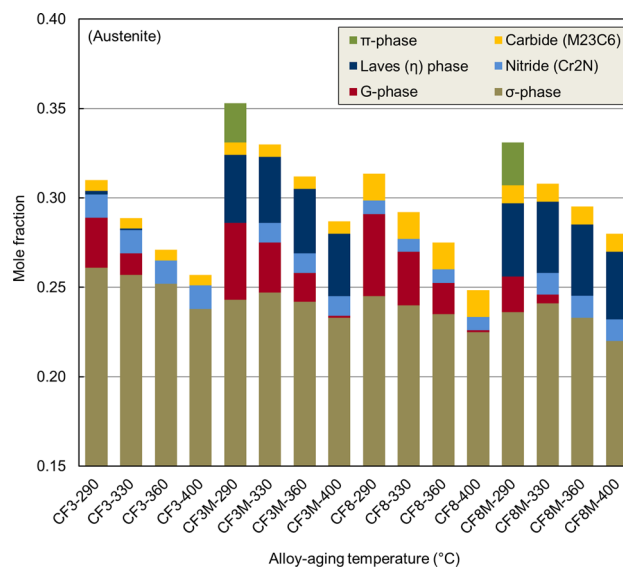


Fig. 5. Precipitation behavior in austenite (γ) phase of CASS materials: the mole fraction data indicate strong dependence on chemistry and aging temperature. Note that the equilibrium amount of σ -phase precipitation might be almost irrelevant to the actual aging behavior in LWR conditions as its formation kinetics is very slow.

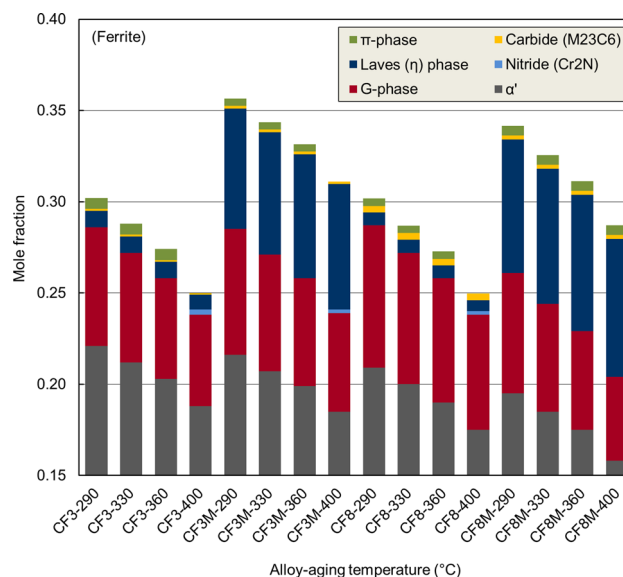


Fig. 6. Precipitation behavior in δ -ferrite phase of CASS materials: the mole fraction data indicate strong dependence on chemistry and aging temperature.

carbide, and π -phase. The discussion below focuses on the temperature and composition dependences of equilibrium precipitation in the respective phases.

It is worth noting that there are other precipitates that may form in CASSs but at a very low rate. These minor phases include M_6C carbide, χ -phase, and R-phase. The M_6C precipitate is a diamond-type fcc carbide and is not very common in austenitic stainless steels as it only forms in certain

compositions.^{30,31} The chi (χ) phase is a bcc crystal that is typically considered as a carbon-dissolving compound that behaves as either an $M_{18}C$ carbide or an intermetallic. A typical composition is $Fe_{36}Cr_{12}Mo_{10}$ and the metallic contents are highly exchangeable.^{29,34} The R-phase is a Mo-rich intermetallic phase with a trigonal crystal structure formed in the ferrite phase of duplex stainless steels or in the grain boundaries.³⁴ Since it is known that these precipitates become practically detectable only at temperatures $>500^{\circ}C$,³¹ their existence was ignored in the calculation and discussion below.

Precipitates in the Austenite (γ) Phase

The major equilibrium precipitates in austenite are σ , G, and Laves phases, although practically the formation of the sigma (σ) phase at low temperature is assumed to be negligible due to its slow formation kinetics.^{29,34,46,47} The sigma (σ) phase is a well-known intermetallic precipitate in Fe-Cr material systems often associated with embrittlement. The σ -phase is a tetragonal crystal composed of $(Cr,Mo)_x(Ni,Fe)_y$, forming always at high-energy interfaces such as triple junction points, grain boundaries, and twin boundaries, and intragranularly at oxide inclusions.⁴⁷ There is some evidence that the σ -phase precipitates only form on previous $M_{23}C_6$ sites or grow where $M_{23}C_6$ precipitates are dissolving.²⁷ This CALPHAD calculation predicted that a large amount of σ -phase ($>20\%$) would be formed in equilibrium and that its mole fraction does not significantly vary with aging temperature and compositional variation in the four alloys, as seen in Fig. 5. Kinetics calculation has predicted, however, that the formation process of σ -phase is much slower than those of the other phases.^{31,46} In a definite time, therefore, the mole fraction of the phase will be very small. This assumption is normally held valid because the nucleation site of sigma is a grain boundary or grain corner that requires a long diffusion distance and fast diffusion rate. Such sluggish formation of the σ -phase suggests that the total amount of precipitates in the austenite matrix after a practical term of aging will be less than that in the δ -ferrite, as mole fractions for other types of precipitate are small in austenite.

More G-phase can be formed at lower temperatures in the simulated range of $250\text{--}450^{\circ}C$ and the mole fraction decreases linearly with temperature. Its mole fraction was 2–5% at $290^{\circ}C$ and became close to zero at slightly above $360\text{--}400^{\circ}C$, depending on the alloy. It appears that the two alloys with relatively low N contents, CF3M and CF8, have formed higher amounts of G-phase, while the lowest amount of G-phase was predicted for the CF8M alloy. G-phase is a Mn-Ni-Si-rich fcc intermetallic phase with a complex composition.^{29,34,48} Carbon is also known to enhance G-phase precipitation. Overall, the G-phase in austenite appears not to be a significant contributor to hardening and loss of toughness in the bulk duplex structure.

Relatively large amounts ($\sim 4\%$) of Laves (η) phase were predicted to form in the austenite phase of CF3M and CF8M alloys containing high Mo contents (2.3 wt.%), while negligible amounts of η -phase are formed in the other two alloys. The histograms for the mole fraction of η -phase show that the η -precipitation depends slightly on aging temperature. The Laves (η) phase particles are hexagonal crystals that are composed of Fe_2Mo in many molybdenum-containing alloys. The Laves phase is often found as small equiaxed particles intragranularly, and occasionally found on the grain boundaries.^{34,37} Usually, the Laves phases are considered detrimental to ductility and fracture toughness, although its actual contribution will be insignificant due to the low mole fraction.

As in many steels, the most common high number density precipitate in CASSs is the $M_{23}C_6$ carbide, where the metal atom (M) is most likely to be chromium.^{29,34} The calculation result shows that this type of carbide forms in all four model alloys and that the mole fraction is nearly temperature independent. As the carbon supply is limited, the amount of $M_{23}C_6$ is mainly determined by C content. The lattice parameters of fcc $M_{23}C_6$ tend to increase with aging temperature and time, reflecting the increase of molybdenum content in carbide.³¹ The $M_{23}C_6$ carbides tend to precipitate at grain boundaries, twin boundaries, and even intragranularly. It is also known that cold working causes the $M_{23}C_6$ precipitates to form at deformation bands and grain boundaries.²⁹

The simpler form of nitride, Cr_2N , precipitates in all alloys with little temperature effect, except that no Cr_2N is formed at $290^{\circ}C$ in Mo-containing alloys (i.e., CF3M and CF8M). Another form of nitride formed is the π -phase, which is a complex nitride form of $Cr_{12.8}(Fe,Ni)_{7.2}N_4$. This form of nitride has been found to precipitate intragranularly in the ferrite phase of duplex stainless steel or in Mn-bearing austenitic stainless steel.³⁴ It has been shown that the mole fraction of the π -phase is retained at more or less 2% up to about $300^{\circ}C$ and then the phase disappears at higher temperatures. No π -phase is predicted at about $350^{\circ}C$ or higher.

Precipitates in the Ferrite (δ) Phase

The major precipitate phase in ferrite is the alpha prime phase (α') followed by the G-phase and Laves phases. Figure 6 shows that the α' -precipitates with a high mole fraction of at least 15% is predicted to form in the δ -ferrite phase of the model alloys. A comparison indicates that the mole fraction in each alloy decreases with aging temperature and a relatively lower amount of martensite is formed in the CF8M alloy. The formation of a Cr-rich α' -phase in high-Cr ferrite has been treated as a key microstructural progress due to its role in the embrittlement mechanism. It is well known that the thermal aging embrittlement of CASS at

temperatures below about 400°C arises primarily as a consequence of a thermally activated separation of chromium by short-range diffusion in the Fe-Cr solid solution of the δ -ferrite phase, resulting in the formation of an iron-rich α phase and a chromium-rich α' phase.^{1-7,29,34} At temperatures <400°C, this process, i.e., Spinodal decomposition, occurs more actively in δ -ferrite and with high chromium contents (>~23%). The α' -phase may also form by nucleation and growth, particularly at temperatures >400°C, but can also contribute at lower temperatures depending on the precise combination of chromium content and temperature e.g. <~26%Cr at 400°C and <~23%Cr at 300°C.^{33,34} An oscillation in the resulting Cr distribution has been observed by high-resolution microscopy techniques with wavelength (in order of nanometers) and amplitude increasing with aging time and temperature.²⁹⁻³⁶ The effect notably increases with the Cr and Mo contents of the ferrite phase, and, consequently, CF8M is less resistant to aging than CF8 or CF3 without Mo.¹⁻⁷ The formation of a brittle α' -phase from δ -ferrite is enhanced by other alloying elements such as silicon which, together with Cr and Mo, can be represented by the chrome equivalent.

The G-phase is the second common phase in ferrite as its mole fraction is retained about 5% or higher at 400°C after a slight decrease from 6% to 8% at 290°C. This indicates that the amount of G-phase in bcc ferrite is not sensitive to the temperature; furthermore, its dependence on alloy composition appears to be negligible. If compared to the amounts in austenite, 0–5%, more G-phase precipitates in the δ -ferrite and at the ferrite–austenite interfaces. It is also noted that the formation of G-phase is more sensitive to temperature in austenite than that in ferrite. The formation of Ni, Si, Mo rich G-phase can reach up to 12% by volume in CASSs. Although the α' -phase is most likely the prime cause for embrittlement in the duplex CASSs, it is believed to aggravate property degradation, as tensile embrittlement solely due to G-phase precipitation has been reported for a single ferrite phase.⁴⁸ This study also reported the G-phase precipitation in a single bcc phase specimen without prior Spinodal decomposition.

Significant amounts of Laves (η) phase (~7%) were predicted to form in the CF3M and CF8M alloys with high Mo contents (2.3 wt.%), while less than 1% forms in the other two alloys (Fig. 6). Since the η -phase is an hcp intermetallics with a nominal chemistry of Fe₂Mo, a larger amount can form in the ferrite phase where both Fe and Mo concentrate.²⁹⁻³⁴ Commonly observed in austenite and ferrite phases, the Laves phase is mainly present in the Mo-doped CF3M and CF8M alloys. Little temperature effect has been observed in the mole fraction of η -phase.

As seen in Fig. 6, all the carbides and nitrides formed in austenite, i.e., M₂₃C₆, Cr₂N, and π -phase (Cr_{12.8}(Fe,Ni)_{7.2}N₄), also precipitate in the ferrite

phase, although those exist commonly in small or negligible amounts. It is worth noting that total mole fractions of equilibrium precipitations in ferrite and austenite are quite similar despite the smaller amounts of these minor phases formed in the ferrite phase. As the carbide and nitride particles tend to precipitate at high energy sites, such as grain boundaries and interfaces where cracks often initiate and propagate, these minor precipitates should have more influence in the cracking process than their larger fractions represent.

CONCLUDING REMARKS

As the past studies indicate, the formation of Cr-rich α' -phase by Spinodal decomposition of δ -ferrite phase is the primary mechanism of thermal embrittlement in cast stainless steels as cracking starts from the decomposed ferrite. It is also known that the smaller carbides and nitrides precipitated at interfaces and grain boundaries provide easier paths for crack propagation. The degree of such embrittlement, however, cannot be conclusively predicted for the extended use of CASS components beyond the current design lifetime, mainly because there is no direct experience over 40 years and because the majority of simulation studies have been accelerated aging experiments at 400°C. The result of thermal activation calculations predicted that a 5-year thermal aging at 330–340°C can simulate the 300°C aging phenomena in the extended service for 60 years and 80 years. On the other hand, the equilibrium calculation results and impact energy data displayed significant aging-temperature-dependence in precipitation behavior and toughness reduction rate in thermal aging. Therefore, the predictability of accelerated aging experiments for assessment of CASS components for extended services is still considered inconclusive. Detailed research needs to confirm that the fundamental mechanisms of microstructural evolution and associated fracture mechanisms are unchanged over the temperature range, including both service temperatures and accelerated aging temperatures. An ultimate goal of the further study should be to provide a knowledge-based conclusive prediction for the integrity of the CASS components in LWR systems during the service life extended up to and beyond 60 years.

ACKNOWLEDGEMENTS

This research was sponsored by U.S. Department of Energy/Office of Nuclear Energy through Light Water Reactor Sustainability (LWRS) Program. Pacific Northwest National Laboratory is operated by Battelle Memorial Institute for the U.S. Department of Energy under Contract No. DE-AC05-76RL01830. The authors would like to express special thanks to Dr. Danny Edwards for his technical reviews and thoughtful comments.

REFERENCES

1. R. Dyle, *Materials Degradation Matrix and Issue Management Tables Overview-LTO Update* (Presented at the Second Workshop on U.S. Nuclear Power Plant Live Extension, Washington, D.C, 2011).
2. Chopra, *Effects of Thermal Aging and Neutron Irradiation on Crack Growth Rate and Fracture Toughness of Cast Stainless Steels and Austenitic Stainless Steel Welds* (NUREG/CR-7185, 2014).
3. K. Chopra and A. Sather, *Initial Assessment of the Mechanisms and Significance of Low-Temperature Embrittlement of Cast Stainless Steels in LWR Systems* (NUREG/CR-5385, 1990).
4. K. Chopra, *Estimation of Fracture Toughness of Cast Stainless Steels during Thermal Aging in LWR Systems* (NUREG/CR-4513, 1991).
5. W.F. Michaud, P.T. Toben, W.K. Soppet, and O.K. Chopra, *Tensile-Property Characterization of Thermally Aged Cast Stainless Steels* (NUREG/CR-6142, 1994).
6. H.M. Chung and T.R. Leax, *Mater. Sci. Technol.* 6, 249 (1990).
7. H.M. Chung, *Evaluation of Aging of Cast Stainless Steel Components* (Presented at ASME Pressure Vessel & Piping Conference, San Diego, CA, 1991).
8. T.S. Byun and J.T. Busby, *Cast Stainless Steel Aging Research Plan* (ORNL/LTR-2012/440, 2012).
9. H.M. Chung, *Presented at the American Society for Mechanical Engineers-Material Properties Council Symposium on Plant Life Extension for Nuclear Components* (Hawaii: Honolulu, 1989).
10. V. Calonne, A.F. Gourgues, and A. Pineau, *Fat. Frac. Eng. Mater. Struct.* 27, 31 (2004).
11. K. Chandra, R. Singhal, V. Kain, and V.S. Raja, *Mater. Sci. Eng. A* 527, 3904 (2010).
12. J.S. Cheon and I.S. Kim, *J. Nucl. Mater.* 278, 96 (2000).
13. F. Danoix, J. Lacaze, A. Gibert, D. Mangelinck, K. Houmada, and E. Andrieu, *Ultramicroscopy* 132, 193 (2013).
14. J.D. Kwon, S.W. Woo, Y.S. Lee, J.C. Park, and Y.W. Park, *Nucl. Eng. Des.* 206, 35 (2001).
15. S. Li, Y. Wang, H. Zhang, S. Li, G. Wang, and X. Wang, *J. Nucl. Mater.* 441, 337 (2013).
16. S. Li, Y. Wang, and X. Wang, *Mater. Sci. Eng. A* 625, 186 (2015).
17. S. Li, Y.L. Wang, H.L. Zhang, S.X. Li, K. Zheng, F. Xue, and X.T. Wang, *J. Nucl. Mater.* 433, 41 (2013).
18. J.E. May, C.A. Caldas de Souza, P.A. de Paula Nascente, P. Soares, C.M. Lepienski, and S.E. Kuri, *Mater. Res.* 13, 431 (2010).
19. M. Murayama, Y. Katayama, and K. Hono, *Metall. Mater. Trans. A* 30A, 345 (1999).
20. F. Xuea, Z.X. Wang, G. Shu, W. Yu, H.J. Shi, and W. Ti, *Nucl. Eng. Des.* 239, 2217 (2009).
21. T. Yamada, S. Okano, and H. Kuwano, *J. Nucl. Mater.* 350, 47 (2006).
22. Y.H. Yao, J.F. Wei, and Z.P. Wang, *Mater. Sci. Eng. A* 551, 116 (2012).
23. X. Lv, S. Li, X. Wang, Y. Wang, Z. Wang, F. Xue, and H. Zhang, *Nucl. Eng. Des.* 280, 493 (2014).
24. ASTM A743/A743M-13, *Standard Specification for Castings, Iron-Chromium, Iron-Chromium-Nickel, Corrosion-Resistant, for General Application.*
25. ASTM A744/A744M-13, *Specification for Castings, Iron-Chromium-Nickel, Corrosion Resistant, for Severe Service.*
26. ASTM A351/A351M-14, *Standard Specification for Castings, Austenitic, for Pressure-Containing Parts..*
27. T.S. Byun and I.S. Kim, *J. Mater. Sci.* 26, 3917 (1991).
28. T.S. Byun and I.S. Kim, *J. Mater. Sci.* 28, 2923 (1993).
29. T. Sourmail, *Mater. Sci. Tech.* 17, 1 (2001).
30. L.P. Stoter, *J. Mater. Sci.* 16, 1039 (1981).
31. B. Weiss and R. Stickler, *Metal Trans.* 3, 851 (1972).
32. J.E. Spruiell, J.A. Scott, C.S. Ary, and R.L. Hardin, *Metal Trans.* 4, 1533 (1973).
33. J. Charles, *Proceedings of Duplex Stainless Steel Conference*, Vol 1 (Les Editions de Physique, Les Ulis Cedex, 1991) pp. 3-48.
34. K.H. Lo, C.H. Shek, and J.K.L. Lai, *Mater. Sci. Eng. R* 65, 39 (2009).
35. P. Hedström, S. Baghsheikhi, P. Liu, and J. Odqvist, *Mater. Sci. Eng. A* 534, 552 (2012).
36. C. Pareige, S. Novy, S. Sallet, and P. Pareige, *J. Nucl. Mater.* 411, 90 (2011).
37. Y. Chen, B. Alexandreanu, and K. Natesan, *Crack Growth Rate and Fracture Toughness Tests on Irradiated Cast Stainless Steels* (ANL-12/56, 2012).
38. O.K. Chopra and W.L. Shack, *Crack Growth Rates and Fracture Toughness of Irradiated Austenitic Stainless Steels in BWR Environment* (NUREG/CR-6960, 2008).
39. O.K. Chopra and W.L. Shack, *Degradation of LWR Core Materials due to Neutron Irradiation* (NUREG/CR-7027, 2010).
40. O.K. Chopra and A.S. Rao, *J. Nucl. Mater.* 412, 195 (2011).
41. Z.B. Wang, N.R. Tao, W.P. Tong, J. Lu, and K. Lu, *Acta Mater.* 51, 4319 (2003).
42. Z.B. Wang, N.R. Tao, W.P. Tong, J. Lu, and K. Lu, *Defect Diffus. Forum* 249, 147 (2006).
43. L. Kaufman, B. Uhrenius, D. Birnie, and K. Taylor, *CALPHAD* 8, 25 (1984).
44. Y. Yang and J.T. Busby, *J. Nucl. Mater.* 448, 282 (2014).
45. W. Cao, S.-L. Chen, F. Zhang, K. Wu, Y. Yang, Y.A. Chang, R. Schmid-Fetzer, and W.A. Oates, *CALPHAD* 33, 328 (2009).
46. T.S. Byun and Y. Yang, *Baseline Characterization of Cast Stainless Steels* (ORNL/TM-2014/446, 2014).
47. J. Barcik, *Mater. Sci. Tech.* 4, 5 (1988).
48. I. Shuro, H.H. Kuo, T. Sasaki, K. Hono, Y. Todaka, and M. Umemoto, *Mater. Sci. Eng., A* 552, 194 (2012).